Body contour 180° pinhole SPET with or without tilted detector: a phantom study

Alain Seret[1], David Flérès[1], Olivier Firket[2], Michel Defrise[3]

[1] Imagerie médicale expérimentale et Centre de Recherche du Cyclotron, Institut de Physique, B5, Université de Liège, Liège 1, Belgium
[2] Radioisotopes, Hopital Erasme, Université Libre de Bruxelles, Brussels, Belgium
[3] Division of Nuclear Medicine, Vrije Universiteit Brussel, Brussels, Belgium

Abstract. This study investigated the feasibility of ordered subsets expectation maximisation (OS-EM) reconstruction of 180° pinhole single-photon emission tomography (SPET) acquired in body contour mode (variable distance between the detector and the axis of rotation for each projection) with or without a tilted detector head. Four non-circular orbits were designed bearing in mind the rotation radius and tilt angle values of previous pin-hole SPET acquisitions in patients with circular orbits. The reconstructions were performed using a dedicated OS-EM algorithm. Reconstructed images of line and uniformity phantoms showed that the spatial and uniformity characteristics of the radioactive objects were preserved. In comparison with the circular orbits, the non-circular orbits allowed only a moderate gain (maximum 10%) in resolution. However, body contour pinhole SPET would significantly facilitate the camera set-up and in this way should decrease the camera set-up time, which is an important parameter in patient studies.

Keywords: Body contour – Pinhole – SPET – Pinhole SPET – OSEM

INTRODUCTION

In the past decade, pinhole single-photon emission tomography (PH SPET) has been a field of intense research work. The initial studies focussed on the development of reconstruction algorithms based on the filtered back-projection approach [1, 2]. Thereafter, iterative reconstruction algorithms such as maximum likelihood expectation maximisation (MLEM) [3, 4] or its accelerated version, ordered subsets expectation maximisation (OSEM) [5], and conjugate gradient (CG) [6] were adapted to the pinhole geometry, with the benefit of superior image quality.

PH SPET was first applied to laboratory small animal studies for which a full 360° orbit appears practical [3, 7, 8]. Such studies are still the main application of PH SPET [8]. The application of PH SPET to humans is limited to bone joints [9, 10] and small organs like the thyroid [6, 11] or the parathyroid glands [10, 12]. Although limited in number, these studies have demonstrated the potential clinical advantages offered by PH SPET. While for some bone joints the 360° circular orbit is still practical, explorations of the shoulder or neck require a 180° orbit [6, 10, 11]. Moreover, optimal resolution in neck PH SPET can only be achieved with a tilted detector [6, 11]. However, even with a tilted detector, the distance between the pin-hole and the neck cannot be minimised for all projections when a circular orbit is used. In our experience, for most projections the pinhole remains far (too far) from the neck. Moreover, the best camera radius of rotation and the best tilt angle are obtained only after a trial and error process involving several camera set-ups, which often seems very long to the patient. This means that the first minutes (sometimes 5–10 min) of the examination are lost in a procedure were no image is acquired. As these minutes generally correspond to the period when the patient is most co-operative, any shortening of the camera set-up period would be highly desirable.

To our knowledge, all PH SPET reconstruction algorithms developed so far impose a circular trajectory. With the aim of keeping the pinhole as close as possible to the target area for all projections and of minimising the camera set-up time, we studied the feasibility of OSEM reconstruction of 180° PH SPET data acquired in body contour mode (variable distance between the detector and the axis of rotation) with or without a tilted detector. A line phantom and a uniformity phantom allowed evaluation of both the achievable resolution and uniformity and the possibility of accurately measuring distances on the reconstructed images. Both phantoms were imaged with circular and non-circular orbits. The results obtained with the non-circular orbits are discussed in the light of the data obtained with the circular ones.

MATERIALS AND METHODS

Camera and pinhole collimator. A Sophy DSX camera (SMV International, Buc, France) was used for all acquisitions. The pin-hole collimator had a height of 205 mm, a circular base diameter of 295 mm and an aperture diameter of 5 mm.

Orbits. Three orbits were defined without tilt and three orbits were defined with a tilt angle of 20° (Fig. 1). These orbits are paired in order that the distance between the pinhole aperture and the axis of rotation (PR) is identical (PR=100 mm) with or without the tilt: two orbits are circular (CO and TCO), two are oblate (OO and TOO) and two are prolate (PO and TPO). The 'T' in the abbreviations denotes a tilted detector head. The values of the tilt angle and of the radius of the circular orbits corresponded to the mean values of the orbits used for 13 patients who had benefited from thyroid PH SPET. Each non-circular orbit was drawn on a cardboard sheet at the 1:1 scale and cut from the sheet in order to obtain a template. In the following, we will use the expression "ideal volume". This ideal volume is defined as the axial extension of the area delimited by the PH orbit and by the straight line connecting its two extremities.

Projection acquisition. The standard procedures for circular or non-circular (body contour) SPET acquisition with a Sophy DSX camera were followed. For a circular orbit, one only needs to define the rotation radius. The desired rotation radius (PR=100 mm) was obtained by varying this parameter until the desired radius value was read on the camera screen. For the non-circular orbits, the template of the orbit was fixed vertically on the camera bed and the orbit was then followed step by step using the camera remote control, allowing the camera to register the desired radius at each rotation step. This is the procedure used for patient studies. Immediately after this set-up procedure, the acquisition computer was switched to the interactive mode and the 32 rotation radii were read from the vector in which they have been stored by the acquisition software. The acquisition computer was then switched to the normal acquisition mode and the acquisition was started. The energy window was centred at 140 keV with a total width of 20%. Thirty-two projections (128×128 images without hardware zoom) per 180° of orbit were acquired.

OSEM reconstruction. The reconstruction algorithm uses a simple voxel-driven back-projector and a ray-driven forward-projector that are tailored for the pinhole geometry and that do not model the finite dimension of the pinhole aperture, the attenuation and the scatter [10]. The back- and forward-projectors allow independent specification of all geometrical parameters for each acquisition angle, including the pinhole focal length, the radius PR, the tilt angle and the 3D location of the orthogonal projection of the pinhole aperture onto the camera. The rest of the software is a straightforward implementation of the OSEM method. The reconstructions were always performed with eight subsets and two iterations. The software allows a free choice of the slice pixel size and of the slice thickness. The reconstructed volume consisted of 128×128×128 voxels. The voxel size was 0.3×0.3×0.3 mm for the resolution and distance measurements and was 1×1×1 mm in all other cases.

Phantoms. Thirteen capillary tubes were filled with an aqueous solution of technetium-99m. These tubes were then glued onto a small Plexiglas drawer in order to obtain a phantom with several parallel lines in the transaxial, coronal and sagittal planes (Fig. 2). With the circular and the PO orbits, this phantom was fully positioned in the ideal volume defined above. With the OO orbit, this was not possible, and the lower part of the phantom stood outside this ideal volume

Fig. 1. *The three paired orbits used in this work and the three orthogonal axis of the image space. CO, Circular orbit; OO, oblate orbit; PO, prolate orbit*

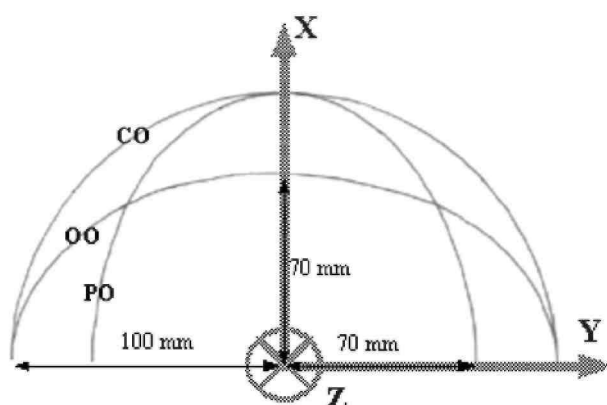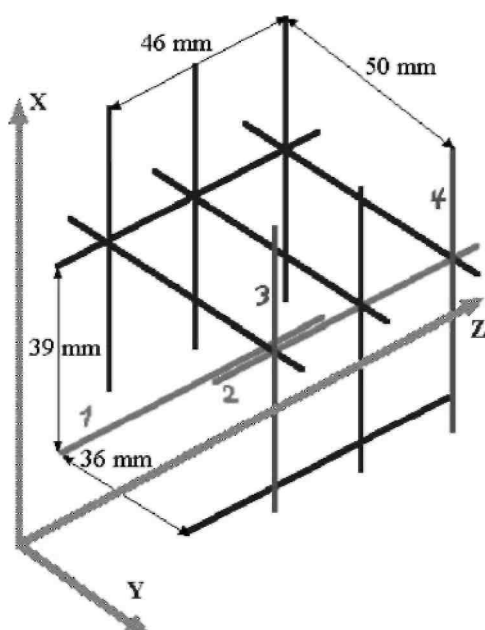**Fig. 2.** *Line phantom used for FWHM and distance measurements together with the three orthogonal axes of the image space. Line 1 lies in the YZ plane at a distance of 18 mm in the Y direction. Line 2 lies in a plane parallel to the YZ plane, at a distance of 18 mm in the Y direction and 39 mm in the X direction. Lines 3 and 4 lie in planes parallel to the XY plane*

.

A cylinder of 70-mm inner diameter and 40-mm inner thickness was constructed in Plexiglas. This cylinder, filled with an aqueous solution of 185 MBq ^{99m}Tc, served as a uniformity phantom. An air bubble was left at the top of the cylinder. This phantom was positioned with its cylindrical axis parallel and close (within 5 mm) to the axis of rotation. Therefore only the half-upper part of the cylinder stood in the ideal volume. The acquisition time per projection was such that at least 200 kcounts per projection were accumulated.

Data analysis. Full-width at half-maximum (FWHM) was measured on count density profiles obtained from the reconstructed slices of the line source phantom. FWHMs were measured in the transaxial plane using line sources 1 and 2 (Fig. 2) and six different transaxial planes covering an axial distance of 40 mm. FWHMs were measured in the axial direction using lines 3 and 4 (Fig. 2) and four coronal slices covering a transaxial distance of 24 mm. The transaxial distances between lines 1 and 2 and the axial distances between lines 3 and 4 (Fig. 2) were also obtained from the count density profiles and taken as the distance between the two profile maxima. These distances were measured on the transaxial and coronal slices used for the FWHM measurements. As there was no systematic variation of the measured FWHM or distance with the plane location, the measurements were averaged and only this mean value is reported. The error on both individual FWHMs and distances between the lines is estimated to be equal to one pixel. The error on the mean FWHM and on the mean distances is calculated as the maximum value of the absolute difference between the individual values and the mean value.

Table 1. *Distances between line sources measured on the reconstructed transverse slices along the two orthogonal axesx andy and on the reconstructed coronal slices along the axis of rotation (z-axis)*

Orbits[a]	Δx (mm)	Δy (mm)	Δz (mm)
CO	37.80±1.50	44.35±1.85	43.75±0.25
PO	36.25±0.95	43.50±1.20	43.50±0.50
OO	38.20±1.60	43.70±1.60	44.00±0.00
TCO	37.90±2.00	42.55±1.55	43.50±0.50
TPO	35.85±1.85	41.30±2.60	45.00±1.00
TOO	37.10±1.00	42.20±1.90	42.35±1.00
True values	39.00±0.50	44.50±0.50	46.00±0.50

[a] Two orbits were circular (CO and TCO), two oblate (OO and TOO) and two prolate (PO and TPO); 'T' denotes a tilted detector head

Table 2. *FWHM of the line sources 1 and 2 measured on the reconstructed transverse slices along the two orthogonal axesx andy and FWHM of the line sources 3 and 4 measured axially (along the z-axis) on the reconstructed coronal slices*

Orbits	Line 1		Line 2		Line 3	Line 4
	FWHMx (mm)	FWHMy (mm)	FWHMx (mm)	FWHMy (mm)	FWHMz (mm)	FWHM z (mm)
CO	7.23±1.53	6.18±0.48	5.95±1.75	5.40±0.30	5.50±0.50	5.50±0.70
PO	5.70±1.20	5.70±1.80	5.33±1.43	5.05±0.20	5.50±0.30	5.50±0.50
OO	6.43±0.88	5.53±0.57	6.08±0.83	5.03±0.38	5.75±1.00	5.50±0.50
TCO	5.75±1.00	5.63±1.73	5.75±1.85	5.55±1.05	5.25±0.85	5.75±0.10
TPO	4.88±0.98	5.53±0.57	5.25±0.45	5.53±0.43	5.50±0.25	6.00±0.45
TOO	5.45±0.55	5.03±0.23	5.55±0.75	4.75±0.40	5.25±0.65	5.85±1.10

The uniformity of the reconstructed images was only assessed visually; no attempt was made to quantify it because it depends on the acquisition and reconstruction matrix size, the acquired count density and the number of subsets and iterations [8].

RESULTS

A 3D maximum intensity view of the reconstructed line source phantom for the six different orbits is presented in Fig. 3. Transverse, sagittal and coronal slices of the reconstructed line source phantom always showed good linearity and parallelism of the lines. Moreover, streak artefacts were not observed on any slice. The measured distances between lines 1 and 2 in the transaxial planes are shown in Table 1 together with the measured axial distances between lines 3 and 4. The results of the FWHM measurements are shown in Table 2.

Transverse slices of the reconstructed uniformity phantom are displayed in Fig. 4 for the orbits without camera head tilt and in Fig. 5 for the orbits with a camera head tilt angle of 20°.

Fig. 3. *3D maximum activity projections of the reconstructed line source phantom for the six different orbits used in this work (see Materials and methods). These 3D views have the same spatial orientation as the phantom sketch in Fig. 2. For the CO and OO orbits, the upper extremity of some vertical lines stood outside the field of view. Each 3D view was generated individually. The absence of smoothing of the reconstructed images and the difference in total number of counts recorded for each orbit were responsible for the slight differences in intensity between the 3D views*
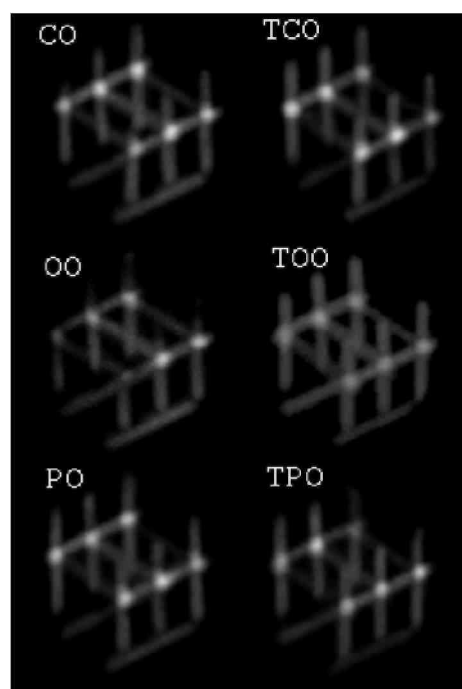
Fig. 4. *Reconstructed transverse slices of the uniformity phantom for the three orbits without camera head tilt used in this work. The slice number gives the axial position in mm of each slice. Slice 60 corresponds to the median plane of the phantom. The arrows point to the area where geometric and uniformity distortions are generated by the use of a 180° orbit instead of a 360° orbit (see text for more details). The maximum of each slice corresponds to the white of the grey colour scale*
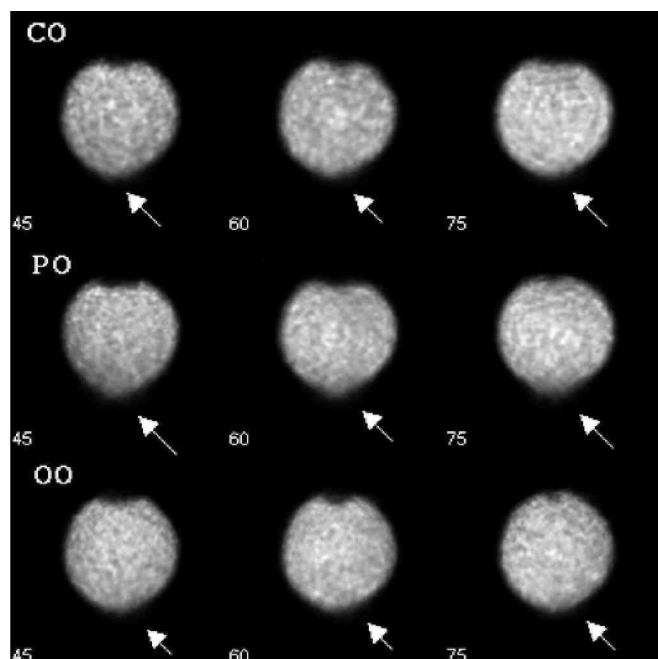

Fig. 5. *Reconstructed transverse slices of the uniformity phantom for the three orbits with camera head tilt of 20° used in this work. The slice number gives the axial position in mm of each slice. Slice 79 corresponds to the median plane of the phantom. The arrows point to the area where geometric and uniformity distortions are generated by the use of a 180° orbit instead of a 360° orbit (see text for more details). The maximum of each slice corresponds to the white of the grey colour scale*
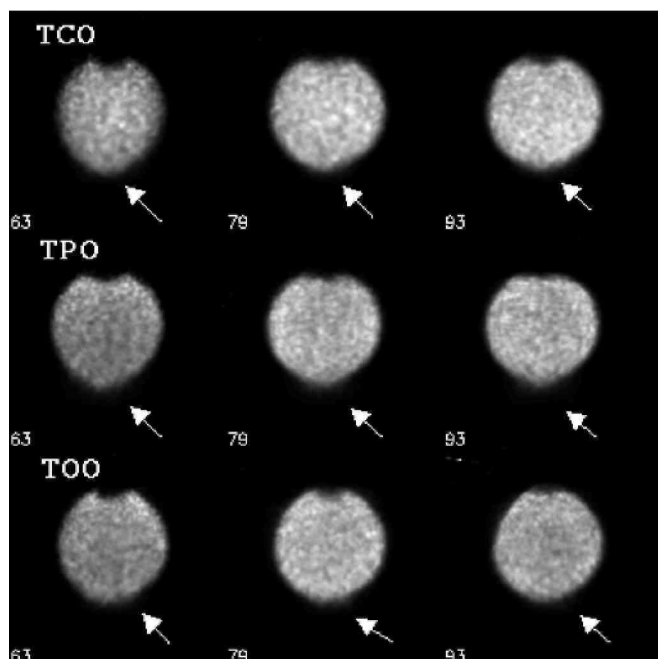

DISCUSSION

Previous studies with PH SPET on humans have mostly used a pinhole aperture diameter of 4 or 5 mm [6, 9, 10, 11, 12]. The pinhole collimators of the Sophy DSX cameras are furnished with aperture diameters of 3, 5 and 7 mm. In our experience, the numbers of counts that can be accumulated in the projections with the 3-mm aperture while keeping a reasonable acquisition time is too low to allow reconstructed images of clinical value, for which

reason the 5-mm aperture was chosen for the present study.

In the case of a circular orbit, its radius is the minimum PR achievable. However, for most of the projections, this PR is not optimal, and the pinhole aperture is far from the neck skin of the patient. Therefore non-circular orbits were designed by progressively shortening the PR in two orthogonal directions (Fig. 1) in order to reach a minimum PR value of 70 mm. The distances between the lines as well as the FWHMs in the transaxial planes were measured along these directions in order to observe any link between the shrinkage direction and the measured value for these two parameters.

The measured distances on the line phantom (Table 1) were very close to the true distances. The largest difference between the measured value and the true value was 8.0% in the axial direction for the orbit TOO. In the transaxial plane, the largest difference was 8.1% and was found for orbit TPO. In a previous work with identical equipment where only circular orbits were used [10], the difference in the transaxial planes amounted to 5.0% for PR=60.8 mm and to 5.6% for PR=110 mm. No axial distance measurement was reported. The largest difference in the transaxial plane found in this work for the circular orbits with PR=100 mm was 4.4%. Although low, these differences seem to be systematic when using this SMV DSX camera. The error amounts to a mean value of 5% for the PR range 6–11 cm. The most probable explanation is a systematic error in the computation of the photon pathlength from its emission point to its impact point in the camera crystal. This computation requires knowledge of the distance between the rotation axis and the pinhole aperture, of the distance from the pinhole aperture to the crystal and of the photon pathlength in the crystal. This last parameter was taken as the mean path of 140-keV photons in NaI crystals. The second parameter could not be measured exactly, because there was a plate covering the crystal. Therefore, we used the value provided by SMV. The first parameter (distance between the rotation axis and the pinhole aperture) is obtained from the camera radius displayed on the camera screen. However, a careful examination of the procedure provided by SMV to perform the camera radius calibration led us to conclude that the precision of the radius value should be in the range 5–10%. In these conditions, it has been estimated that an error of 5% on the measured distance is acceptable. The existence of this error means that the geometric zooming factor provided by the pin-hole collimator is slightly underestimated. Therefore the FWHM discussed below are also probably slightly underestimated. As mentioned above, the magnitude of the underestimation seems not to depend on the PR value.

Most of the FWHMs measured for the circular orbits (Table 2) were in the range 5–6 mm. They were in the same range as the FWHM obtained previously with identical equipment and PR radius [10] except for the FWHM of line 1 along x with the CO orbit. The 7.23mm value for this FWHM exceeded by more than 1 mm the previous measurements [10] and the other FWHMs obtained in this work. It should be noted that a different phantom with only two lines was used in the previous work [10]. One line was lying on the rotation axis and the second line was close to the position of line 2 in this work, so that no measurement could be performed at a location close to line 1.

The FWHMs obtained with the non-circular orbits were similar to the corresponding FWHM obtained with the circular orbit (Table 2). With the non-circular orbits, the pinhole aperture gets closer to the object and we therefore expect a better spatial resolution (in the x direction for the PO orbit or in the y direction for the OO orbit). This is confirmed by the results in Table. 2: the difference between the FWHM in the transaxial plane obtained with the non-circular and with the corresponding circular orbit was small compared to the error, but it was generally negative. Each non-circular orbit used in this work was created by shrinkage of the circular orbit in one direction. Nevertheless, the FWHMs measured along the two orthogonal shrinkage directions remained close (within about 0.5 mm) to each other. With the patients, the differences between the non-circular orbit and a circular orbit will generally be less systematic in direction so that it can be expected that the FWHM will remain more isotropic in the case of patient studies.

For the uniformity phantom, the mean count numbers per pixel were much higher than the mean count numbers that could be obtained in the patient studies. The uniformity of the reconstructed images of these phantoms was satisfactory for all orbits (Figs. 4, 5), excepting some non-uniformity and geometric distortions (arrows in Figs. 4 and 5) in the area opposed to the ideal volume. Comparable distortions have been previously reported [10] and are due to the fact that the half-lower part of the phantom extends beyond the limit of the ideal volume. It can be observed that the distortions affect only the bottom of the lower part of the phantom, an area located at 30–35 mm from the ideal volume lower limit. Ideally, the target area of the patients should be fully located in the ideal volume [10]. The images presented in Figs. 4 and 5 show that there is about 3 cm of tolerance to this rule. This is important for patient studies because the location of the target area is not always exactly known.

The air bubble that was left at the top of the uniformity phantom to mimic a cold nodule was clearly visible. This observation confirmed the absence of geometric distortion in the ideal volume, as already observed with the line phantom. Moreover, the reconstructed slices from the circular and the non-circular orbits were very similar. Therefore the use of the non-circular orbits seems not to alter the uniformity of OSEM PH SPET reconstructed

image.

The recording of only 32 projections for a 180° orbit is theoretically suboptimal for 3D tomographic reconstruction. However, the images presented in this work, as well as the images presented in other works [6, 10], are free of streak artefacts, spatial distortions or uniformity defects. Therefore, it seems that this low number of projections is sufficient when the reconstruction is performed with an iterative algorithm. The projection data are sufficient for accurate reconstruction in the plane of the PH orbit provided the tracer distribution in that plane is confined to the ideal area delimited by the PH orbit and by the straight line connecting its two extremities. In contrast, accurate PH reconstruction is impossible outside the central plane, even with a 360° orbit. Therefore increasing artefacts should be expected in planes located at an increasing distance from the central plane. However, examination of Figs. 3, 4 and 5 does not reveal large differences between the central slice (slice of the pinhole orbit) and the other slices. Moreover, the distance and FWHM were measured on different slices of the line phantom, and no systematic differences between the values obtained on the slice comprising the PH orbit and the other slices were observed.

The main difficulty encountered in the present study derived from the Sophy DSX camera, which was 10 years old. For non-circular orbits, the rotation radii are not stored in the projection file header and have to be extracted from the computer memory before starting the acquisition. This procedure takes several minutes and would be impractical with patients; however, it would not be required with more recent scanners, which generally store the radii in the headers of the data files.

In body contour PH SPET, it is always important to monitor the persistence screen of the camera during the set-up procedure to check that the target area remains within the field of view for all projections. This requirement sometimes limits the distance between the patient skin and the pinhole aperture to a value larger than the minimum physical value of this parameter.

In conclusion, OS-EM reconstruction of body contour 180° pinhole SPET with or without a tilted detector head has been shown to be feasible. On the reconstructed images of line and uniformity phantoms, the spatial and the uniformity characteristics of the radioactive objects are preserved. The only difference noticed between the images obtained with circular and non-circular orbits is a moderate gain in resolution. In clinical practice, the use of non-circular orbits should often decrease considerably the tomography set-up time of the camera.

References

1. Palmer J, Wollmer P. Pinhole emission computed tomography: method and experimental evaluation. *Phys Med Biol* 1990; 21:339–350.
2. Li J, Jaszczak RJ, Greer KL, Coleman RE. A filtered-backpro-jection algorithm for pin-hole SPECT with a displaced center of rotation. *Phys Med Biol* 1994; 39:165–176.
3. Jaszczak RJ, Li J, Wang H, Zalutsky MR, Coleman RE. Pin-hole collimation for ultra-high-resolution, small-field-of-view SPECT. *Phys Med Biol* 1994; 39:425–437.
4. Scarfone C, Jaszczak RJ, Li J, Soo MS, Smith MF, Greer KL, Coleman RE. Breast tumour imaging using incomplete circular orbit PH SPET: a phantom study. *Nucl Med Commun* 1997; 18:1077–1086.
5. Vanhove C, Defrise M, Franken PR, Everaert H, Deconinck F, Bossuyt A. Interest of the ordered expectation maximisation (OS-EM) algorithm in pinhole single-photon emission tomography reconstruction: a phantom study. *Eur J Nucl Med* 2000; 27:140–146.
6. Desvignes P, Laurette I, Koulibaly PM, Migneco O, Bussière F, Darcourt J. An algebraic 3D reconstruction method for pin-hole SPECT: validation for cold thyroid nodule detection. *Eur J Nucl Med* 2000; 27:942.
7. Weber DA, Ivanovic M. Ultra-high-resolution imaging of small animals: implications for preclinical and research studies. *J Nucl Cardiol* 1999; 6:332–344.
8. Habraken JBA, de Bruin K, Shehata M, Booij J, Bennink R, van Eck Smit BLF, Busemann Sokole E. Evaluation of high-resolution pinhole SPECT using a small rotating animal. *J Nucl Med* 2001; 42:1863–1869.
9. Bahk YW, Chung SK, Park YH, Kim SH, Lee HK. Pinhole SPECT imaging in normal and morbid ankles. *J Nucl Med* 1998; 39:130–139.
10. Seret A, Defrise M, Blocklet D. 180° pinhole SPET with a tilted detector and OS-EM reconstruction: phantom studies and potential clinical applications. *Eur J Nucl Med* 2001; 23: 1836–1841.
11. Wanet PM, Sand A, Abramovici J. Physical and clinical evaluation of high-resolution thyroid pinhole tomography. *J Nucl Med* 1996; 37:2017–2020.
12. Gabriel M, Erler H, Profanter C, Moncayo R, Riccabona G. Evaluation of parathyroid nodules with thallium/technetium pinhole SPECT. *Eur J Nucl Med* 2000; 27:1070.